

Accepted Manuscript

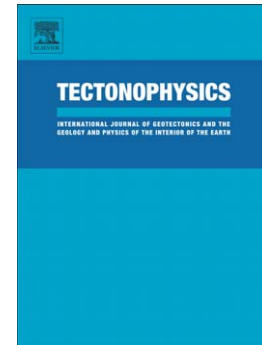
Marine magnetotellurics imaged no distinct plume beneath the Tristan da Cunha hotspot in the southern Atlantic Ocean

Kiyoshi Baba, Jin Chen, Malte Sommer, Hisashi Utada, Wolfram H. Geissler, Wilfried Jokat, Marion Jegen

PII: S0040-1951(16)30406-1
DOI: doi:[10.1016/j.tecto.2016.09.033](https://doi.org/10.1016/j.tecto.2016.09.033)
Reference: TECTO 127265

To appear in: *Tectonophysics*

Received date: 29 February 2016
Revised date: 11 September 2016
Accepted date: 29 September 2016



Please cite this article as: Baba, Kiyoshi, Chen, Jin, Sommer, Malte, Utada, Hisashi, Geissler, Wolfram H., Jokat, Wilfried, Jegen, Marion, Marine magnetotellurics imaged no distinct plume beneath the Tristan da Cunha hotspot in the southern Atlantic Ocean, *Tectonophysics* (2016), doi:[10.1016/j.tecto.2016.09.033](https://doi.org/10.1016/j.tecto.2016.09.033)

This is a PDF file of an unedited manuscript that has been accepted for publication. As a service to our customers we are providing this early version of the manuscript. The manuscript will undergo copyediting, typesetting, and review of the resulting proof before it is published in its final form. Please note that during the production process errors may be discovered which could affect the content, and all legal disclaimers that apply to the journal pertain.

Marine magnetotellurics imaged no distinct plume beneath the Tristan da Cunha hotspot in the southern Atlantic Ocean

Kiyoshi Baba^{a,*}, Jin Chen^b, Malte Sommer^b, Hisashi Utada^a, Wolfram H. Geissler^c, Wilfried Jokat^{c,d}, and Marion Jegen^b

^a Earthquake Research Institute, The University of Tokyo, 1-1-1 Yayoi, Bunkyo-ku, Tokyo 113-0032, Japan

^b GEOMAR, Helmholtz Centre of Ocean Research Kiel, Wischhofstr. 1-3, 24148 Kiel, Germany

^c Alfred Wegener Institute, Helmholtz Centre for Polar and Marine Research Bremerhaven, Am Alten Hafen 26, 27568 Bremerhaven, Germany

^d University of Bremen, Geoscience department, Bremen, Germany

* Corresponding author.

E-mail addresses: kbaba@eri.u-tokyo.ac.jp, jchen@geomar.de, msommer@geomar.de, utada@eri.u-tokyo.ac.jp, Wolfram.Geissler@awi.de, Wilfried.Jokat@awi.de, mjegen@geomar.de

ABSTRACT

The Tristan da Cunha (TDC) is a volcanic island located above a prominent hotspot in the Atlantic Ocean. Many geological and geochemical evidences support a deep origin of the mantle material feeding the hotspot. However, the existence of a plume has not been confirmed as an anomalous structure in the mantle resolved by geophysical data because of lack of the observations in the area. Marine magnetotelluric and seismological observations were conducted in 2012–2013 to examine the upper mantle structure adjacent to TDC. The electrical conductivity structure of the upper mantle beneath the area was investigated in this study. Three-dimensional inversion analysis depicted a high conductive layer at ~120 km depth but no distinct plume-like vertical structure. The conductive layer is mostly flat independently on seafloor age and bulges upward beneath the lithospheric segment where the TDC islands are located compared to younger segment south of the TDC Fracture Zone, while the bathymetry is rather deeper than prediction for the northern segment. The apparent inconsistency between the absence of vertical structure in this study and geochemical evidences on deep origin materials suggests that either the upwelling is too small and/or weak to be resolved by the current data set or that the upwelling takes place elsewhere outside of the study area. Other observations suggest that 1) the conductivity of the upper mantle can be explained by the fact that the mantle above the high conductivity layer is depleted in volatiles as the result of partial melting beneath the spreading ridge, 2) the potential temperature of the segments north of the TDC Fracture Zone is lower than that of the southern segment at least during the past ~30 Myr.

Highlights

The electrical structure beneath the Tristan da Cunha (TDC) hotspot was investigated.
 Plume-like structure was not imaged beneath TDC by 3-D inversion analysis.
 The plume may be small and/or weak or take place elsewhere outside of the study area.
 Conductivity and bathymetry anomalies show a contrast across the TDC fracture zone.
 Mantle temperature and melting process at ridge may cause the conductivity anomaly.

Keywords

Marine magnetotellurics
 Electrical conductivity
 Upper mantle
 Hotspot
 Tristan da Cunha
 Atlantic Ocean

1. Introduction

Tristan da Cunha (TDC) islands are currently active hotspot volcanoes in the South Atlantic Ocean. The islands are located at the southwestern, youngest end of the aseismic Walvis Ridge. The landfall of Walvis Ridge at the Namibian coast is connected to a continental flood basalt (CFB) province or large igneous province (LIP) erupted ~132 Ma, named Etendeka Plateau (Figure 1). These geological features seem to support the idea that the TDC hotspot is a surface manifestation of an upwelling or plume from deep in the mantle underneath a moving oceanic plate and that the plume played a role in the opening of the southern Atlantic Ocean. Courtillot et al. (2003) classified the origin of the TDC hotspot as this type of a deep or ‘primary’ plume from the time-progressive volcanic trails with the LIP, and large buoyancy represented by topographic swell although a high noble gas isotope ($^3\text{He}/^4\text{He}$) ratio and a seismic low velocity anomaly at ~500 km depth are not observed in TDC hotspot area. Anderson (2005) suggested the TDC hotspot has its origin in rather shallower tectonic processes according to his scoring criteria for hotspots. O’Connor et al (2012; 2015) discussed the contribution of both plume and plate tectonic processes on the formation of the hotspot trails in the South Atlantic based on the ages of seamounts and the background seafloor. The Walvis Ridge topography splits into a Tristan trail that ends at the TDC islands and a Gough trail that ends at Gough Island located ~400 km southeast of the TDC islands. The geochemical signatures based on trace element and Sr-Nd-Hf-Pb isotope data suggest that the TDC hotspot is fed by a plume originated from the core-mantle boundary and a chemical zonation of the plume with a source of the Tristan trail relatively more depleted than that of the Gough trail (Hoernle et al., 2015; Rohde et al., 2013).

Geophysical observations can help the discussion about the hotspot source, giving a current snapshot of the mantle structure, which Courtillot et al. (2003) and Anderson (2005) used as a plume index. Seismic velocity is primarily dependent on the temperature of the mantle and thus a low velocity anomaly may be interpreted as a high temperature anomaly. Electrical conductivity is another observable physical property that is also controlled by ambient temperature but in a different way than seismic velocity. Both properties are also sensitive in some sense to the presence of partial melt and the chemical states. Especially, recent laboratory experiments indicate that electrical conductivity of mantle minerals such as olivine and melt are sensitive to the volatiles H_2O and CO_2 dissolved therein (e.g., Gardés et al., 2015; Sifré et al., 2014). These are also thought to be more enriched in oceanic island basalt (OIB) sources, i.e. plume feeding of hotspot volcanoes (Hirschmann and Dasgupta, 2009). Therefore, the use of either or both observations provides useful information on thermal and chemical states of the mantle, which can give critical hints to distinguish the possible hotspot sources. However, the observations based on global (but mostly land-based) networks are inadequate to resolve the local structure especially for the upper mantle beneath the TDC hotspot area, which is located in the very middle of the Atlantic Ocean. Regional observations have never been conducted before in the vicinity of TDC hotspot. The conflict in the discussion on the TDC hotspot source can be attributed at least partly to a lack of the direct geophysical observations.

Regional campaign observation using seafloor instruments is thus indispensable to understand the physical processes associated with the TDC hotspot. We conducted a marine geophysical experiment around the TDC islands as a part of German South Atlantic Margin Processes and Links with onshore Evolution (SAMPLE) project (<https://www.sample-spp.de/>). The observations include passive seismological and electromagnetic (EM) observations, detailed bathymetry and gravity mapping in the area. Ocean bottom seismometers (OBSs) and ocean bottom electromagnetometers (OBEMs) were deployed in January, 2012 and recovered in January, 2013 using the German research vessel R/V Maria S. Merian. Data acquisition was conducted for almost one year. The OBS/OBEM array covered an area of approximately 550 km in the east-west direction and 350 km in the north-south direction centered on TDC Island (Figure 1). The survey area is located east of the Mid-Atlantic Ridge with seafloor ages between 10 and 30 Myr. The TDC islands are located on a seafloor with an age of ~22 Myr. Running east-west just south of the TDC islands is the TDC Fracture Zone with a ~3 Myr age gap between its northern (older) and southern (younger) segments. Detailed bathymetric and gravity data were collected around the OBS/OBEM sites and major topographic features by shipboard multi-narrow beam echo sounding (MBES) system and gravimeter during the deployment and recovery cruises.

This paper presents the first result on the EM part of the marine geophysical observations for the TDC hotspot. The magnetotelluric (MT) analysis of the observed EM data gives information of the

electrical conductivity distribution of the upper mantle beneath the survey area. In the following sections, we describe the EM observation and data analysis, the resulting three-dimensional (3-D) electrical conductivity model, and discuss major features of the model. Seismic observations are reported elsewhere (Geissler et al., submitted to Tectonophysics; Schloemer et al., submitted to Earth and Planetary Science Letters). The joint interpretation of all observations that is our ultimate goal will be carried out in the near future.

2. Observation and data analysis

The EM observation was carried out through a collaboration of German and Japanese research groups: GEOMAR, Helmholtz Centre of Ocean Research Kiel and Earthquake Research Institute (ERI), The University of Tokyo, who supplied 18 and 8 OBEMs to the experiment, respectively. The OBEMs were equipped with a fluxgate magnetic sensor and two orthogonal electric dipoles to measure the time variation of the natural EM field. The GEOMAR OBEMs recorded data every 10 seconds for maximum 240 days. The ERI OBEMs recorded every 60 seconds for the entire period from the deployment to the recovery (340–350 days). Three of the ERI OBEMs, which were deployed near the TDC islands where the water is relatively shallow, started the measurement with 10 second sampling and switched to 60 second sampling after one month. At these locations we expected to be able to collect shorter period data, which is absorbed stronger due to the skin effect at locations with larger water depth. Seafloor EM sites were distributed with a spacing of ~100 km and of approximately 50 km spacing in the vicinity of TDC islands. We also deployed a land MT instrument, which was supplied by the Geophysical Instrument Pool of GFZ, Helmholtz Centre Potsdam, on Nightingale Island (NTG). We succeeded to recover all sites (see Table 1 for details). Meaningful data acquisition failed at two seafloor sites, Tris09 and Tris22, and one island site (NTG). For Tris09 and Tris22, the magnetic field data were too noisy to recover the orientation of the instrument and thus the electric field data were not available, either. NTG failed to record magnetic field data correctly. The data from the other 24 sites were used for the following analysis although some of them have unavailable field component and/or time sections. They were first manually cleaned for abnormal fluctuations such as spikes and steps, and then corrected for the instrumental clock drift and the coordinate system. We also used the magnetic field data at the TDC Island, which was collected by DTU Space, Denmark and provided by INTERMAGNET (<http://www.intermagnet.org>) for data processing.

The MT impedance tensor, which is a transfer function between the horizontal electric field and horizontal magnetic field components, was estimated for each site from the quality controlled time series data, using a bounded influence algorithm with generalized remote reference method (Chave and Thomson, 2004). For Tris05, Tris18, Tris20, Tris23, and Tris25, where only magnetic field data were available, electric fields recorded at adjacent sites were used. We accounted for this by using

corresponding electric and magnetic field data in the forward modeling and inversion analysis. The TDC observatory data were used for the remote reference to reduce the effect of site-dependent noise in the seafloor magnetic field data.

Examples of the obtained MT responses are shown as apparent resistivity and phase as a function of period in Figure 2. The major off-diagonal elements show a feature typical for seafloor MT responses with an initial apparent resistivity increase at small periods which then decrease with increasing period. This feature can be attributed to a sequence (or layering) of relatively conductive oceanic crust, a highly resistive oceanic lithospheric mantle, and a conductive asthenospheric and deeper mantle. The difference between xy and yx elements and non-zero xx and yy elements indicates the presence of lateral variation of the electrical conductivity. Remarkable features were observed in the shorter period range at sites in the vicinity of the TDC islands, for example, Tris11 and Tris26. The diagonal apparent resistivities can be in part comparable to or even larger than the off-diagonal elements and the phases vary more than 90 degrees. These features are typical for 3-D conductivity variations, which may arise either from the strong 3-D topography and/or from a subsurface lateral heterogeneity in the conductivity.

The 3-D electrical conductivity structure of the subsurface was estimated from the MT responses taking into consideration the effect of topography by procedures described in detail in previous studies (Baba et al., 2010; Baba et al., 2013a, Tada et al., 2012; 2014). The procedures used are described briefly below. One-dimensional (1-D) structure was first estimated by the method proposed by Baba et al. (2010) and then a 3-D inversion was applied to all observed MT responses using the 1-D model as initial and prior models (Baba et al., 2013a; Tada et al., 2014). A good initial guess of a starting model is rather critical for 3-D inversion of MT data, since it ensures stable and fast convergence. To obtain a more reliable 3-D subsurface structure, it is important to take into account the effect of topography for both the initial 1-D and subsequent 3-D analyses. The topographic effect that we consider in this study includes local small-scale topographic variations in the vicinity of the sites resolved by 150 m mesh MBES data and regional large-scale topography resolved by 1 arc-minute mesh ETOPO1 (Amante and Eakins, 2009). Figure 3 shows the discretized topography models for the regional and local scale. For the regional topography, we use a 25 km grid cell in an area of 350 km \times 350 km in the study area and larger cells in the outer area that includes far continental coasts (Figure 3a). For the local model, we use a 1 km mesh for modeling the topography in an area of in the central 7 km \times 7 km area and larger meshes in the outer 350 km \times 350 km area (Figure 3b). Topographic effects both of regional and local scales were simulated by the so-called 2-stage forward modeling (Baba et al., 2013a). Hereafter the forward response including both topographic effects and subsurface structure is referred to as Z^{ts} . We applied error floors of 2.5% for the off diagonal elements and 5.0% (but the absolute value of 0.01 $\mu\text{V}/\text{m}/\text{nT}$ for the periods shorter than 3,000 s) for the diagonal elements of the MT impedance throughout the 1-D and 3-D

inversion analyses. The error floor values were chosen based on the experiential accuracy of the 3-D forward modeling. Applying the error floor aims to avoid overfitting to the data that is meaningless in terms of the accuracy of the forward modeling.

A 1-D model was estimated by an iterative approach of 1-D inversion of the data and topographic effect correction (see Baba and Chave, 2005 and Baba et al., 2010 for detailed description of procedure). Data used for the 1-D inversion were calculated by the square root of the determinant of the MT impedance at each site and then averaged over all sites for each period. The standard error of the averaged response was calculated from those for each site based on the error propagation law to which we then applied a 2.5% error floor. However, five sites, which were located in the vicinity of TDC (Tris05, Tris11, Tris12, Tris18, and Tris26) were excluded in the averaging because they show strongly abnormal features caused by strong local topography. For these sites, the phase changes more than 90 degrees with period. Such a feature cannot be reconstructed by any 1-D model based on EM theory. The averaged response was then inverted using Occam's inversion method (Constable et al., 1987) to a 1-D earth model. The target root-mean-squared (RMS) misfit was set to 1.7 to avoid unrealistically rough structures. In a first step, the MT response was simulated by 3-D topography over the 1-D subsurface structure (\mathbf{Z}^{ts}). In a second step, the topographic effect on the MT impedance was calculated from the initial 3-D response \mathbf{Z}^{ts} and 1-D forward $\mathbf{Z}^{1\text{-D}}$, and the observed MT responses, \mathbf{Z}^{obs} , were corrected for the effect using $\mathbf{Z}^{\text{cor}} = \{\mathbf{Z}^{\text{ts}} \mathbf{Z}^{1\text{-D}}\}^{-1} \mathbf{Z}^{\text{obs}}$. The corrected responses were then averaged again and submitted to the next iteration of the 1-D inversion. The iteration was stopped when the RMS misfit between \mathbf{Z}^{ts} and \mathbf{Z}^{obs} was not reduced by following iterations.

A 3-D model was estimated by an iterative 3-D inversion approach using the local small-scale topographic effect term update (Baba et al., 2013a; Tada et al., 2014). Within this 3-D inversion sequence, we applied the derived topographic effect to the modeled 3-D data rather than correct the observed responses such that the observed (non-corrected) MT responses, \mathbf{Z}^{obs} , were inverted. The horizontal dimension of the 3-D model is identical to the sub-area (1,656 km \times 1,656 km) of the large topography model (Figure 3a). The forward part of the 3-D inversion calculates the MT responses to this regional large-scale structure (hereafter referred to as \mathbf{Z}^{rs}), such that \mathbf{Z}^{rs} does not include local small-scale topography effects and far-field topography outside of the inversion model. The MT response to the total structure (the full topography over the 1-D model), \mathbf{Z}^{ts} , was separately simulated just for the initial model by the independent 2-stage forward modeling mentioned above. \mathbf{Z}^{ts} was then input to the 3-D inversion, and the distortion, \mathbf{D} , due to the local small-scale and the far topography, which is expressed by 2×2 complex-valued tensor, was calculated from \mathbf{Z}^{ts} and \mathbf{Z}^{rs} by $\mathbf{D} = \mathbf{Z}^{\text{ts}} \mathbf{Z}^{\text{rs}-1}$ at the beginning of the inversion. The reason why we introduced this approach is because the direct modeling of \mathbf{Z}^{ts} requires more computational time and thus it should be avoided in the 3-D inversion in which runs many forward calculations. \mathbf{D} was fixed and the data misfit was evaluated between \mathbf{Z}^{obs} and $\mathbf{D} \mathbf{Z}^{\text{rs}}$ through the inversion iterations. This means that mutual coupling between the

distortion and subsurface structure is assumed to be negligibly small. The assumption is, however, not always reasonable. Therefore, we re-calculated \mathbf{Z}^{ts} to the model consisting of the full topography over the resultant 3-D model and ran the 3-D inversion again updating \mathbf{D} by new \mathbf{Z}^{ts} and using the previous inversion result as the new initial and prior models. These processes were iterated several times. At each update step, we evaluated the RMS misfit between \mathbf{Z}^{obs} and \mathbf{Z}^{ts} , which is free from the mutual coupling problem. We found it was still hard to model the strong topographic effect for Tris11 (See Figure 2) by the current inversion scheme so that a part of the Tris11 data (responses at the periods shorter than 1000 s) were excluded from the 3-D inversion analysis.

3. Results

The averaged MT responses and the 1-D models before and after the topographic effect correction are shown in Figure 4. Both 1-D models show a relatively conductive uppermost layer, a highly resistive layer at around 30 km depth, a conductive layer at around 130 km depth, and a gradual increase in the conductivity with depth below ~250 km depth. The topographic effect correction changed the MT response only slightly. The difference is mostly visible in the longer periods, which is probably due to far continental coast effect although the effect is quite small compared to those observed in other areas (e.g., Baba et al., 2010; Baba et al., 2013b). The 1-D model also became slightly more resistive at depths of 20–100 km and 200–400 km but high conductivities with $\sim 0.07 \text{ S m}^{-1}$ at ~130 km depth remained after the topographic correction. The difference is almost insignificant if we consider the 95% limit of the model uncertainty. More iterations did not change the result. The MT impedances were calculated to the model consisting of the topography over the final 1-D model by the 2-stage forward modeling. The normalized residuals between \mathbf{Z}^{ts} and \mathbf{Z}^{obs} are plotted in Figure 5a.

The 3-D electrical conductivity model was then estimated by the scheme described above. The 3-D inversion and the topographic distortion update were iterated 11 times until the convergence and the 3-D model achieved the chosen minimum RMS misfit at 10th iteration (Figure 6). The RMS misfit was reduced from 4.69 for the optimum (initial) 1-D model to 4.15 for the best 3-D model. Figure 5b demonstrates that the normalized residuals are reduced for all four elements of the MT impedance tensors and they distribute more symmetrically to zero. The apparent resistivity and phase calculated for the 3-D model explains well the overall features of our observation (Figure 2).

Our final 3-D electrical conductivity model is shown in Figure 7. The most important finding is that the model does not show any remarkable sub-vertical structure resembling a plume conduit beneath the TDC islands. This is somewhat surprising since the mantle plume is thought to be hotter and/or rich in volatiles and thus it is expected to be electrically more conductive than the surrounding mantle. The obtained structure of our 3D model is mainly horizontally layered although there are some lateral variations visible in the model. The mantle at depths between ~50 and ~230

km has a lateral variation larger than half an order of magnitude in conductivity and its variation is a maximum (~ 1 order of magnitude) at ~ 90 km depth (Figure 8). The horizontal slices at 80 and 120 km depths in Figure 7 show relatively resistive zones north of the TDC islands and at the southern edge of the observation array. A relatively conductive band is sandwiched by these resistive zones; in other words, the high conductivity layer exhibits a bulge there. The boundary between the southern resistive zone and the central conductive band is rather linear especially at shallow (80 km) depths and runs parallel to the TDC Fracture Zone. The deeper part of the upper mantle and the mantle transition zone exhibit less lateral variations.

4. Sensitivity tests

We tested if a vertical conductor rising from the mantle transition zone is really unnecessary or not to explain our data through forward modeling. The best 3-D model was modified to include a vertical conductor (modified model A). Previous studies on electrical conductivity structure beneath the Hawaiian and Society hotspots in Pacific suggested conductive anomalies (e.g., Nolasco et al., 1998; Simpson, 2000; Constable and Heinson, 2004) although they gave only limited discussion in the anomaly as a 3-D body since their data covered only a limited area of the hotspot region. Constable and Heinson (2004) obtained a two-dimensional electrical conductivity model across the Hawaiian hotspot swell. In their model, the conductive anomaly appears beneath the Hawaii Island down to the lower mantle. The anomaly was as conductive as $\sim 0.1 \text{ S m}^{-1}$ ($10 \text{ } \Omega\text{m}$) and its diameter is ~ 200 km or less. Recent work on the Society hotspot revealed more significant conductive anomaly by the similar 3-D inversion analysis to this study (Tada et al., submitted to Nature Geoscience). The anomaly extends from the mantle transition zone upwards to ~ 50 km depth. The conductivity reaches to $\sim 1 \text{ S m}^{-1}$ at the center of the anomaly and the diameter is ~ 200 km. In accordance with these studies, we chose a conductivity value of 0.316 S m^{-1} ($3.16 \text{ } \Omega\text{m}$) and a diameter of ~ 200 km for our superimposed anomaly (Figure 8). MT responses at all observation sites were then simulated using the 2-stage forward modeling and compared with our observations. The total RMS misfit increased to 4.28 for modified model A. RMS misfits for sites increased although there are some exceptional sites (Figure 9a). The increase of the RMS was seen in most of the MT impedance tensor elements (Table 2, suggesting that the change in the total RMS misfit cannot be attributed to few bad data points but to an overall change in the feature of MT responses for the modified model. The increase of the total RMS misfit is statistically significant in terms of F -test with 95% confidence limit. We therefore concluded that our data set should be able to distinguish between an existence or non-existence of such a distinct vertical conductor. We also investigated the effect of smaller diameters (~ 150 km, ~ 100 km) and smaller conductivity anomalies (0.1 S m^{-1}) of the vertical conductor. In these cases, we did not obtain significant changes in the RMS misfit such that we cannot exclude the presence of a smaller vertical conductivity anomaly based on our data.

The sensitivity to the undulation of the high conductivity layer was also tested by the forward modeling. The conductivity of the central conductive zone, the northern and southern resistive zones at depth between ~60 km and ~200 km are replaced by the respective mean value in the shown area. We refer to these models as modified model B1, B2, and B3, respectively (Figure 9b). The resultant RMS misfits for these modified models are 4.26, 4.18, and 4.17. The misfit increase is statistically significant only for the modified model B1, as would be anticipated since MT is generally more sensitive to conductive anomalies. The increase in the RMS misfit is larger for most of the sites and elements for the modified model B1 but relatively smaller for the modified models B2 and B3 (Figure 9b and Table 2). These results indicate that for example at 80 km depth, the conductivity values of maximum $\sim 0.14 \text{ S m}^{-1}$ in the conductive zone is likely and the resistive anomalies do not have to be more resistive than $\sim 0.05 \text{ S m}^{-1}$. The relative undulation of the conductivity in the depths should therefore be reliable although the intensity especially in the resistive side is not well constrained.

5. Discussion

The electrical conductivity structure of the oceanic upper mantle has frequently been discussed in terms of the relation with the lithospheric cooling with age. The seafloor age of the study area is 10–30 Myr and therefore the 1-D model represents a mantle of this age interval. We compared the 1-D model with a model obtained from the Philippine Sea (Baba et al., 2010) and a model predicted from expected thermal structure for the similar age (Figure 8). The predicted model was calculated from a thermal profile for 10–30 Myr old mantle based on the half-space cooling with the potential temperature of $1350 \text{ }^{\circ}\text{C}$ and $0.3 \text{ }^{\circ}\text{C km}^{-1}$ adiabatic temperature gradient and the electrical conductivity of hydrous olivine model obtained from compilation of laboratory measurements (Gardés et al., 2015). The electrical conductivity profiles were calculated for 0 ppm and 100 ppm water content in olivine.

We cannot draw a clear conclusion from the two observation based models at 30 Myr. The 1-D models for TDC and the Philippine Sea are significantly different. The upper resistive layer of the TDC mantle is thicker than that of the Philippine Sea mantle. Defining the representative value of the resistive-to-conductive boundary as 0.01 S m^{-1} , the boundary depth is $\sim 80 \text{ km}$ for the TDC mantle and $\sim 50 \text{ km}$ for the Philippine Sea mantle. The maximum conductivity is also significantly different. The peak conductivity of 0.07 S m^{-1} was observed at $\sim 140 \text{ km}$ depth for the TDC mantle while it was 0.03 S m^{-1} at $\sim 80 \text{ km}$ depth for the Philippine Sea mantle. For the depths between 200 and 300 km, both models show similar conductivity of $\sim 0.03 \text{ S m}^{-1}$. The differences in the models may be attributed to different geodynamic settings in the respective locations. The Philippine Sea is a back arc basin and thus the physical and chemical states of the mantle structure might reflect influence of mantle wedge dynamics associated with the subduction process. In case of TDC, the

physical and chemical states may be affected by the hotspot process.

The TDC 1-D model at 20–70 km depths agrees well with the predicted 1-D model for dry olivine. Below ~70 km depth, the TDC 1-D model is significantly more, i.e. anomalously, conductive. The higher conductivity may be attributed to higher temperature, volatiles such as water and carbon dioxide, and/or existence of melt. The conductivity common to the two observed profiles at 200–300 km depth is yet again well explained by a hydrous olivine model for which the water content of 100 ppm is typical for the mid-ocean ridge basalt (MORB) source mantle (e.g., Hirschmann, 2010). The depths around the conductivity peak require additional factors enhancing the conductivity. The facts above suggest that the TDC model supports the idea of the volatiles redistribution because of the generation of partial melting beneath spreading ridges. We discuss this issue further with the 3-D model in the following paragraphs.

The thermal structure of the upper mantle in the study area should change with the distance from the Mid-Atlantic Ridge if it obeys a simple cooling with age due to the thermal conduction. To investigate the effect of the temperature gradient on model, we calculated a 3-D conductivity model based a 3-D thermal structure. The latter was derived based on the simple 1-D half-space cooling with seafloor ages at the locations in the study area and the electrical conductivity of dry olivine was calculated for the thermal structure (Figures 10b and 10e). Figures 10c and 10f-l show the residual of the model in log resistivity after the dry olivine model was subtracted from that of the 3-D inversion model. In the vertical sections parallel to the seafloor spreading direction (Figures 10j-l), we identify a flat, high conductivity layer at around 120 km depth although the thickness of the thermally conductive layer varies from ~20 km in the west to ~90 km in the east of the study area, depending on the age. The resistive-to-conductive boundary is clearly depicted at 60–70 km depths at least in the western half of the study area. The resistivity above 60–70 km depths is comparable or even higher than that of olivine. The uppermost part of the residual structure is strongly negative because dry olivine model is very resistive at these depths compared to the inversion model (Figure 8). The large mismatch at shallow depths can be explained by the fact that MT data are generally insensitive to the actual conductivity value in the shallow resistive region.

The features described above support the idea of a compositional rather than a thermal control on the electrical conductivity for the young oceanic upper mantle. The mantle peridotite dissolves some amount of volatiles such as H₂O and CO₂, which are supposed to enhance the bulk conductivity. The volatiles should be extracted effectively into melt when the mantle material ascends crossing the depth of the dry peridotite solidus (60–70 km) beneath the spreading ridge. As a result, depleted material spreads at the depth shallower than this dry solidus depth and the depletion can remain constant with age because of extremely slow diffusion of hydrogen (Hirth & Kohlstedt, 1996). Below the dry solidus depth, the mantle is more conductive because the peridotite is still hydrated and/or because small amount of carbonated hydrous incipient melt may exist (Hirschmann 2010).

This hypothesis was first confirmed from the MT observation on very young (< 5 Myr) seafloor near the East Pacific Rise (Evans et al., 2005; Baba et al., 2006). Baba (2005) predicted based on the hypothesis that the age-independent high conductivity layer can be observed in the seafloor younger than ~ 30 Myr. The result in this study presents another example of a good agreement with this prediction. It is also worth noting that the hypothesis holds for a slow spreading system such as the Mid-Atlantic Ridge for this study as well as for the other end member, the fast spreading East Pacific Rise. There is an exceptional example in terms of this scenario in the world. Naif et al. (2013) studied young (23–24 Myr) oceanic mantle beneath Cocos plate, off Nicaragua and found much thinner (~ 45 km) resistive layer and much higher ($0.17\text{--}0.25\text{ S m}^{-1}$) conductive peak below the resistive layer. Their model was explained by relatively higher potential temperature of 1420°C , higher H_2O content of 275 ± 85 ppm, and higher fraction (1.0–2.1 %) of partial melt than those assumed for typical oceanic mantle (Hirschmann, 2010). It is apparently inconsistent with the compositional boundary scenario because the higher thermal profile crosses the dry mantle solidus at greater depths causing a thicker resistive layer. Additional processes like that the melt migrates upward (maybe because of higher melt fraction) and pools beneath less permeable lithosphere in off ridge would be necessary to explain this observation, as Naif et al. (2013) pointed out.

The high conductivity layer bulges beneath the lithospheric segment on which TDC islands are located, except for an area north of TDC islands (Figures 7 and 10). The southern edge of the bulge is nearly parallel to the TDC Fracture Zone as can be recognized more clearly from the plot of iso-depth of the resistivity anomaly (Figure 11c). Due to the age difference of about 3 Myr, the TDC islands lithospheric segment should have a thicker thermal boundary layer than the adjacent younger segment south of the TDC Fracture Zone. Therefore, we would expect a lower conductivity in the TDC islands' segment than in the southern segment, i.e., depression of the high conductivity, if only the thermal effect would be taken into account. Bathymetry data can give a hint to interpret this apparent inconsistency. We calculated the bathymetry anomaly to the prediction based on the subsidence due to the half-space cooling with age (Figure 11a). If we consider only features of relatively long spatial wavelengths, we notice that the bathymetry anomaly in the northern segment is higher (deeper) than that of the southern segment.

We suggest that the mantle potential temperature is lower in the northern segment relative to the southern segment at least in the past ~ 30 Myr to explain the undulation in the high conductivity layer and the bathymetry (Figure 12). Under the assumption that the potential temperature is lower, the thermal profile crosses the dry peridotite solidus at shallower depths and thus the compositional boundary, namely the top of the high conductivity layer, becomes shallower. Also, the bathymetry subsidence is larger for lower potential temperature. If this is the case, this study presents the first result based on the seafloor MT that discovered the variation in the mantle potential temperature along the past spreading axis. The potential temperature should affect the crustal thickness as well.

The hotter potential temperature generates more melt beneath the ridge and yields thicker crust (e.g., Klein & Langmuir, 1987). Crustal thickness based on seismological observations was derived around the TDC islands through receiver function analysis (Geissler et al., submitted to Tectonophysics). Based on their study, crustal thicknesses vary between 5.5 and 7 km for both, the segments north and south of the TDC Fracture Zone, although the correlation with the supposed potential temperature difference for the two segments is not clear. The amount and certainty of observations are probably too small to discuss any correlation in greater detail. Further studies are necessary to give more quantitative interpretation.

The resistive anomaly north of TDC islands is difficult to explain. The resistivity can be as resistive as that of olivine down to ~100 km depth, that is deeper than the depth of dry solidus. Although higher resistivities are not well constrained by the data as tested in the previous section, we can make an attempt to interpret this feature. Lower potential temperature and depletion in H₂O and CO₂ could explain these increased resistivities. This interpretation would be somewhat supported by a small deeper bathymetry anomaly that is located in the part of the resistive anomaly area (Figure 11a and 11b), which also suggests a lower potential temperature to some degree. However, if the mantle in this area is enriched in H₂O and CO₂ as in the surrounding area, lower potential temperature rather makes the compositional boundary shallower as discussed above. Therefore, a depleted and (at least partly) cooler region is a more likely explanation for the resistive anomaly, yet why the region would be more depleted is unknown.

The 3-D model obtained in this study does not support the existence of a strong vertical conductor plume beneath TDC, which is comparable in terms of conductivity and the conduit diameter with that observed beneath the Society hotspot (Tada et al., submitted to Nature Geoscience). However, there are a lot of geochemical evidences suggesting that the mantle material is fed by a deep seated source (e.g., Hoernle et al., 2015; Rohde et al., 2013). The high conductivity at ~120 km depth suggests the contribution of volatiles and melting. One possible explanation is that upwelling exists, but is too small and/or weak to be observed. We cannot rule out a small, less hot, and/or less volatile enriched upwelling indicative of a (dying) plume, since it would be beyond the resolution of our data.

Another possibility explaining the lack of a vertical plume signature is that the plume takes place elsewhere and the deep mantle materials flow within the asthenospheric mantle horizontally to feed the TDC volcanism. One of the possible alternative locations for the upwelling is south of TDC islands, where seismic receiver functions indicate relatively hot and thin mantle transition zone (Geissler et al., submitted to Tectonophysics). Other possibilities are Gough Island or a location between TDC and Gough Island. Gassmöller et al. (2016) succeeded to reconstruct the evolution of the complex crust thickness pattern of the Walvis Ridge and the Tristan and Gough trails, taking account for the global westward mantle flow and ridge-plume interactions. In their modeling the

upwelling was assumed in the middle point between the TDC and Gough Islands. To prove these possibilities, additional observations covering wider area are necessary.

6. Conclusions

The marine MT experiment was conducted around the TDC hotspot in 2012–2013. The observed data were carefully analyzed with taking into account for the topographic effect to estimate a 3-D electrical conductivity structure model of the upper mantle beneath the area.

The obtained model does not support a distinct plume-like vertical conductor beneath the TDC hotspot although many previous geological and geochemical studies suggest the upwelling from deep (lower) mantle. Apparent inconsistency with these studies suggests that the current plume is so small, less hot, and/or less enriched in the volatiles that our MT data could not resolve it or that the upwelling takes place elsewhere out of the study area and feeds the recent volcanoes by horizontal flow.

The 3-D conductivity model shows a high conductive layer at around 120 km depths that is flat independently on seafloor age. Because the coincidence of the depth of the resistive-to-conductive boundary and dry peridotite solidus at 60–70 km, the feature can be explained by the fact that the mantle above the boundary is depleted in volatiles as the result of partial melting beneath the spreading ridge.

The high conductive layer bulges beneath the segment north of the TDC Fracture Zone which is ~3 Myr older than the southern segment. The bathymetry of the northern segment is somewhat deeper than predicted by the half-space cooling model. These observations can be explained by the lower potential temperature beneath the northern segment at least in the past ~30 Myr.

The model also shows a resistive anomaly in the north of TDC, which is as resistive as dry olivine down to 100 km depth. This feature suggests that the mantle is depleted in volatiles although the reason is unknown.

Acknowledgements

We thank the captain Ralf Schmidt and the crew of R/V Maria S. Merian for the professional and friendly support of the scientific work in the cruises. Patrick Schröder, Olav Schwartz, Martin Wollatz-Vogt, and Toyonobu Ota are also thanked for their technical assistance on the OBEMs. The compilation of the MBES data collected in the cruises was helped by Gesa Barkawitz, Janina Kammann, Irena Schulten, and Marcia Maia. Comments from two anonymous reviewers helped to improve the manuscript. All figures were produced using Generic Mapping Tools (Wessel et al., 2013). This work was supported by the German Research Foundation (DFG) grant JE296/9-1 as part of the Priority Program SPP1375, the Future Ocean program of Kiel Marine Sciences, and the Grant-in-Aid for Scientific Research (KAKENHI) 23403005 of Japan Society for the Promotion of

Science (JSPS).

References

- Amente, C., Eakins, B.W., 2009. ETOPO1 1 arc-minute global relief model: Procedures, data sources and analysis. NOAA Tech. Memo. NESDIS NGDC-24, National Geophysical Data Center, Marine Geology and Geophysics Division, Boulder, Colorado, 19pp.
- Anderson, D.L., 2005. Soring hotspots: The plume and plate paradigms. in Foulger, G.R., Natland, J.H., and Anderson, D.L., eds., *Plates, plumes, and paradigms: Geological Society of America Special Paper 388*, 31–54, doi:10.1130/2005.2388(04).
- Baba, K., 2005. Electrical structure in marine tectonic settings. *Surv. Geophys.*, 26, 701–731, doi:10.1007/s10712-005-1831-2.
- Baba, K., Chave, A.D., 2005. Correction of seafloor magnetotelluric data for topographic effects during inversion. *J. Geophys. Res.*, 110, B12105, doi:10.1029/2004JB003463.
- Baba, K., Chave, A.D., Evans, R.L., Hirth, G., Mackie, R.L., 2006. Mantle dynamics beneath the East Pacific Rise at 17 °S: Insights from the Mantle Electromagnetic and Tomography (MELT) experiment. *J. Geophys. Res.*, 111, B02101, doi:10.1029/2004JB003598.
- Baba, K., Utada, H., Goto, T., Kasaya, T., Shimizu, H., Tada, N., 2010. Electrical conductivity imaging of the Philippine Sea upper mantle using seafloor magnetotelluric data. *Phys. Earth Planet. Inter.*, 183, 44–62, doi:10.1016/j.pepi.2010.09.010.
- Baba, K., Tada, N., Utada, H., and Siripunvaraporn, W., 2013a. Practical incorporation of local and regional topography in three-dimensional inversion of deep ocean magnetotelluric data, *Geophys. J. Int.*, 194, 348–361, doi:10.1093/gji/gg115.
- Baba, K., Tada, N., Zhang, L., Liang, P., Shimizu, H., Utada, H., 2013b. Is the electrical conductivity of the northwestern Pacific upper mantle normal? *Geochem. Geophys. Geosyst.*, 14(12), 4969–4979, doi:10.1002/2013GC004997.
- Chave, A.D., Thomson, D.J., 2004. Bounded influence magnetotelluric response function estimation. *Geophys. J. Int.*, 157, 988–1006, doi:10.1111/j.1365-246X.2004.02203.x.
- Constable, S.C., Parker, R.L., Constable, C.G., 1987. Occam's inversion: A practical algorithm for generating smooth models from electromagnetic sounding data. *Geophysics*, 52(3), 289–300.
- Constable, S., and Heinson, G., 2004. Hawaiian hot-spot swell structure from seafloor MT sounding, *Tectonophysics*, 389, 111–124, doi:10.1016/j.tecto.2004.07.060.
- Courtillot, V., Davaille, A., Besse, J., Stock, J., 2003. Three distinct types of hotspots in the Earth's mantle. *Earth Planet. Sci. Lett.*, 205, 295–308.
- Evans, R.L., Hirth, G., Baba, K., Forsyth, D., Chave, A., Mackie, R., 2005. Geophysical evidence from the MELT area for compositional controls on oceanic plates. *Nature*, 437, 249–252, doi:10.1038/nature04014.

- Gardés, E., Gaillard, F., Tarits, P., 2015. Toward a unified hydrous olivine electrical conductivity law. *Geochem. Geophys. Geosyst.*, 15, 4984–5000, doi:10.1002/2014GC005496.
- Gassmüller, R., Dannberg, J., Bredow, E., Steinberger, B., Torsvik, T.H., 2016. Major influence of plume-ridge interaction, lithosphere thickness variations and global mantle flow on hotspot volcanism – The example of Tristan. *Geochem. Geophys. Geosyst.*, 17, 1454–1479, doi:10.1002/2015GC006177.
- Geissler, W.H., Jokat, W., Jegen, M., Baba, K. Thickness of the oceanic crust and the mantle transition zone in the vicinity of the Tristan da Cunha hot spot estimated from ocean-bottom and ocean-island seismometer receiver functions, submitted to *Tectonophysics*.
- Hirschmann, M.M., Dasgupta, R., 2009. The H/C ratios of Earth's near-surface and deep reservoirs, and consequences for deep Earth volatile cycles. *Chem. Geology*, 262, 4–16, doi:10.1016/j.chemgeo.2009.02.008.
- Hirschmann, M.M., 2010. Partial melt in the oceanic low velocity zone. *Phys. Earth Planets. Inter.*, 179, 60–71, doi:10.1016/j.pepi.009.12.003.
- Hirth G., Kohlstedt, D.L., 1996. Water in the oceanic upper mantle: implications for rheology, melt extraction and the evolution of the lithosphere. *Earth Planet. Sci. Lett.*, 144, 93–108.
- Hoernle, K., Rohde, J., Hauff, F., Garbe-Schönberg, D., Homrighausen, S., Werner, R., Morgan, J.P., 2015. How and when plume zonation appeared during the 132 Myr evolution of Tristan Hotspot. *Nature Comm.*, 6, 1–10, doi:10.1038/ncomms8799.
- Klein, E.M., Langmuir C.H., 1987. Global correlations of ocean ridge basalt chemistry with axial depth and crustal thickness. *J. Geophys. Res.*, 92(B8), 8089–8115.
- Müller, R.D., Sdrolias, M., Gaina, C., Roest, W.R., 2008. Age, spreading rates, and spreading asymmetry of the world's ocean crust. *Geochem. Geophys. Geosyst.*, 9(4), Q04006, doi:10.1029/2007GC001743.
- Naif, S., Key, K., Constable, S., and Evans, R.L., 2013. Melt-rich channel observed at the lithosphere-asthenosphere boundary, *Nature*, 495, 356–359, doi:10.1038/nature11939.
- Nolasco, R., Tarits, P., Filloux, J.H., and Chave, A.D., 1998. Magnetotelluric imaging of the Society Islands hotspot, *J. Geophys. Res.*, 103(B12), 30,287–30,309.
- O'Connor, J.M., Jokat, W., le Roex, A.P., Class, C., Wijbrans, J.R., Keßling, S., Kuiper, K.F., Nebel, O., 2012. Hotspot trails in the South Atlantic controlled by plume and plate tectonic processes. *Nature Geoscience*, 5, 735–738, doi:10.1038/ngeo1583.
- O'Connor, J.M., Jokat, W., 2015. Age distribution of Ocean Drill sites across the Central Walvis Ridge indicates plate boundary control of plume volcanism in the South Atlantic. *Earth Planet. Sci. Lett.*, 424, 179–190, doi:10.1016/j.epsl.2015.05.021.
- Rohde, J., Hoernle, K., Hauff, F., Werner, R., O'Connor, J., Class, C., Garbe-Schönberg, Jokat, W., 2013. 70 Ma chemical zonation of the Tristan-Gough hotspot track. *Geology*, 41(3), 335–338,

- doi:10.1130/G33790.
- Sifré, D., Garés, E., Massuyeau, M., Hashim, L., Hier-Majumder, S., Gaillard, F., 2014. Electrical conductivity during incipient melting in the oceanic low-velocity zone. *Nature*, 509, 81–85., doi:10.1038/nature13245.
- Simpson, F., Steveling E., and Leven, M., 2000, The effect of the Hawaiian plume on the magnetic daily variation, *Geophys. Res. Lett.*, 27(12), 1775–1778.
- Sleep N.H., 2002. Local lithospheric relief associated with fracture zones and ponded plume material. *Geochem. Geophys. Geosyst.*, 3(12), 8506, doi:10.1029/2002GC000376.
- Schlömer, A., Geissler, W.H., Jokat, W., and Jegen M., Hunting for the Traistan Mantle Plume – An upper mantle tomography around the volcanic island of Tristan da Cunha, submitted to *Earth, Planets Sci. Lett.*
- Tada, N., Baba, K., Siripunvaraporn, W., Uyeshima, M., Utada, H., 2012. Approximate treatment of seafloor topographic effects in three-dimensional marine magnetotelluric inversion. *Earth Planets Space*, 64, 1005–1021, doi:10.5047/eps.2012.04.005.
- Tada, N., Baba, K., Utada, H., 2014. Three-dimensional inversion of seafloor magnetotelluric data collected in the Philippine Sea and the western margin of the northwest Pacific Ocean. *Geochem. Geophys. Geosyst.*, 15, 2895–2917, doi:10.1002/2014GC005421.
- Tada, N., Tarits, P., Baba, K., Utada, H., Kasaya, T., Suetsugu, D., Electromagnetic evidence for volatile-rich upwelling beneath the Society hotspot. submitted to *Nature Geoscience*.
- Wessel, P., Smith, W. H. F., Scharroo, R., Luis, J., Wobbe F., 2013. Generic Mapping Tools: improved version released. *Eos, Trans. AGU*, 94(45), 409–410.

Figure captions

Figure 1. Bathymetric map and observation array. Bathymetry data were constructed by merging ETOPO1 (Amante and Eakins, 2009) and MBES data collected on the deployment and recovery cruises MSM 20-2 and MSM24. Crosses with “Tris” label and numbers indicate the location of the seafloor observation sites. TDC is a geomagnetic observatory on TDC Island. NTG is an MT site on Nightingale Island deployed in this campaign. Contour lines indicate seafloor age (Müller et al., 2008). Inset shows region of the study area, outlined by a yellow rectangle. Major tectonic features are also indicated: EP (with a red star), Etendeka Plateau; GI (with a red star), Gough Island; GFZ, Gough Fracture Zone; MAR, Mid-Atlantic Ridge; TDCI (with a red star), Tristan da Cunha Island; TDCFZ, Tristan da Cunha Fracture Zone; and WR, Walvis Ridge.

Figure 2. MT responses in terms of the log apparent resistivity and impedance phase (symbols with error bars) along the line crossing near the TDC Island in East-West direction. Colors correspond to elements of the MT impedance tensor as shown in the legend, in which x and y are geographical north and east direction, respectively. The error bars are one standard error but the error floors were applied (see text). The solid lines are the responses calculated from the 3-D inversion model shown in Figure 7. Data in the shaded period range for Tris11 were not used in the 3-D inversion due to severe topographic effects noticeable in the data.

Figure 3. (a) Regional large-scale topography model. Red rectangle indicates the horizontal dimension of the model for calculation of \mathbf{Z}^{rs} in the 3-D inversion. The topography model was created from ETOPO1. Yellow rectangle is the area encompassing the 3-D conductivity structure models plotted in Figures 7, 9, 10 and 11. (b) An example of the local small-scale topography model for Tris21. The topography models were created from the data that merged ETOPO1 and the MBES data. Crosses indicate the location of the OBEM site.

Figure 4. Averaged MT responses (left) and 1-D electrical conductivity structure models (right) before (blue) and after (red) topographic effect correction. Solid lines in left panels are responses predicted from the 1-D models shown in the right panel. For the final model, model uncertainties for 70 and 95% limits are shown as light and heavy red shades, respectively.

Figure 5. Residuals between observed and calculated MT impedances for all sites, normalized by observation errors (error floors were applied). RMS misfits were calculated for each element. (a) and (b) show the residuals for our best fitting 1-D and 3-D models, respectively.

Figure 6. Variation of the RMS misfit between \mathbf{Z}^{obs} and \mathbf{Z}^{ts} with the topographic distortion term (\mathbf{D}) update iterations. The mantle structure is the 1-D model at the 0th iteration. At each iteration, the 3-D inversion was run using the mantle model obtained by the previous inversion as initial and prior

models, subsequently a 2-stage forward modeling was run to calculate \mathbf{Z}^{ts} . The best RMS misfit is indicated by a gray circle.

Figure 7. 3-D electrical conductivity model. (a) to (f) show horizontal slices at different depths. (g) to (l) show vertical sections along lines $A-A'$ to $F-F'$. Colors indicate resistivity values (inverse of conductivity) in log scale. Crosses denote sites used for 3-D inversion analysis, gray contour lines outline bathymetry. White dashed lines represent the depths or profiles of the horizontal slices or the vertical sections.

Figure 8. Comparison of 1-D profiles. Red line denotes the 1-D model (identical to the one shown in Figure 4). Red shade represents the range of lateral variation (in the area shown in Figure 7) of the 3-D model. Green line is the 1-D model of the Philippine Sea mantle obtained by Baba et al. (2010). Blue line shows prediction from a thermal structure model between 20 and 30 Myr old mantle and laboratory based electrical conductivity model for dry olivine (see text for detail), cyan line for olivine dissolving 100 ppm water.

Figure 9. Modified 3-D model (A) used for sensitivity test to a vertical conductor (a) and undulation of the high conductivity layer at around 120 km depth (b). In (b), the central conductive zone (left; model B1), the northern resistive zone (center; model B2), and the southern resistive zone (right; model B3) were modified. Top panels are the horizontal slices and the bottom panels are the vertical sections. Note that the vertical sections in (b) are vertically exaggerated by a factor of 2 for clarity. The corresponding change in RMS misfits for each site from those models relative to our best 3-D model (ΔRMS) are plotted by colored crosses. White dashed lines represent the depths or profiles of the horizontal slices or the vertical sections. Bathymetric contour lines are depicted similarly as in Figure 7.

Figure 10. 3-D resistivity anomaly to a synthetic 3-D model that is predicted from a thermal structure based on simple 1-D half-space cooling with age at arbitrary positions and dry olivine conductivity. (a), (b), and (c) are the horizontal slices at 80 km depth of the 3-D inversion model, the synthetic model, and the residual between the two, respectively. (d), (e), and (f) are the same as (a), (b), and (c) but at 120 km depth. Observation sites and bathymetry are plotted in same notation as in Figure 7. (g) to (l) show vertical sections of the residual along the lines $A-A'$ to $F-F'$. Gray lines denote isotherm. Note that the vertical direction is exaggerated by a factor of 2 for clarity.

Figure 11. (a) Bathymetry anomaly to the prediction from the simple 1-D half-space cooling thermal structure. (b) Resistivity anomaly at 80 km depth, in identical form as in Figure 10c. (c) Iso-depth distribution of the resistivity anomaly of -0.5 log unit. The observation sites and bathymetry are as in Figure 7. Dotted line indicates the location of the TDC Fracture Zone.

Figure 12. Schematic idea of the mantle temperature variation along the Mid-Atlantic Ridge that can explain the difference in the resistivity and bathymetry anomalies across the TDC Fracture Zone.

ACCEPTED MANUSCRIPT

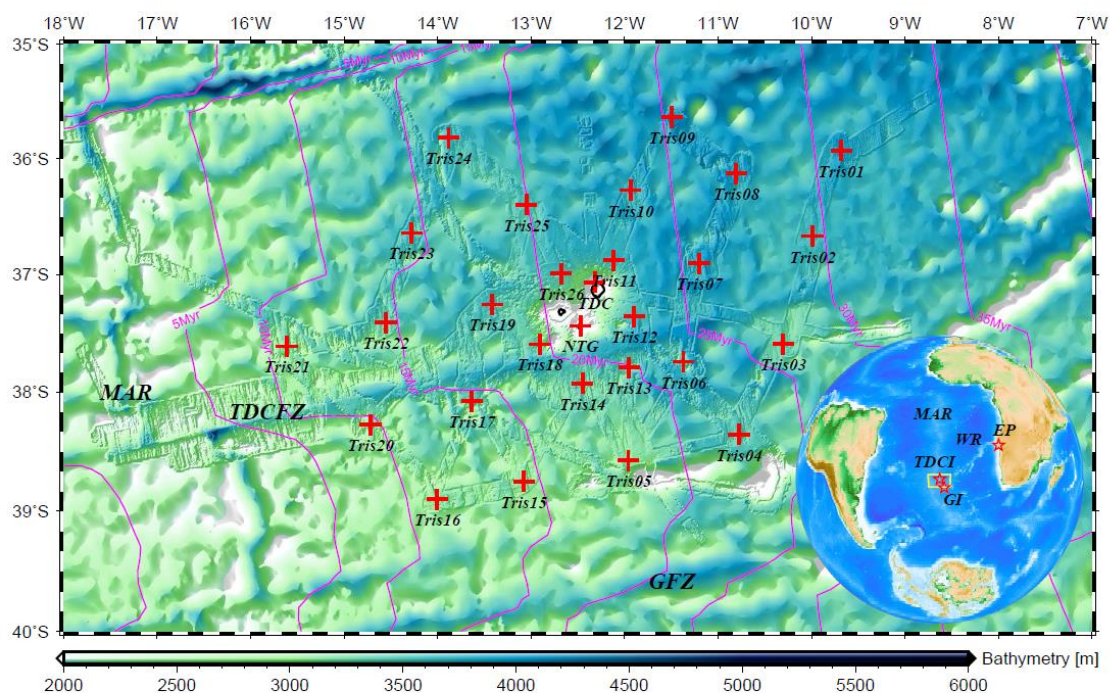


Fig. 1

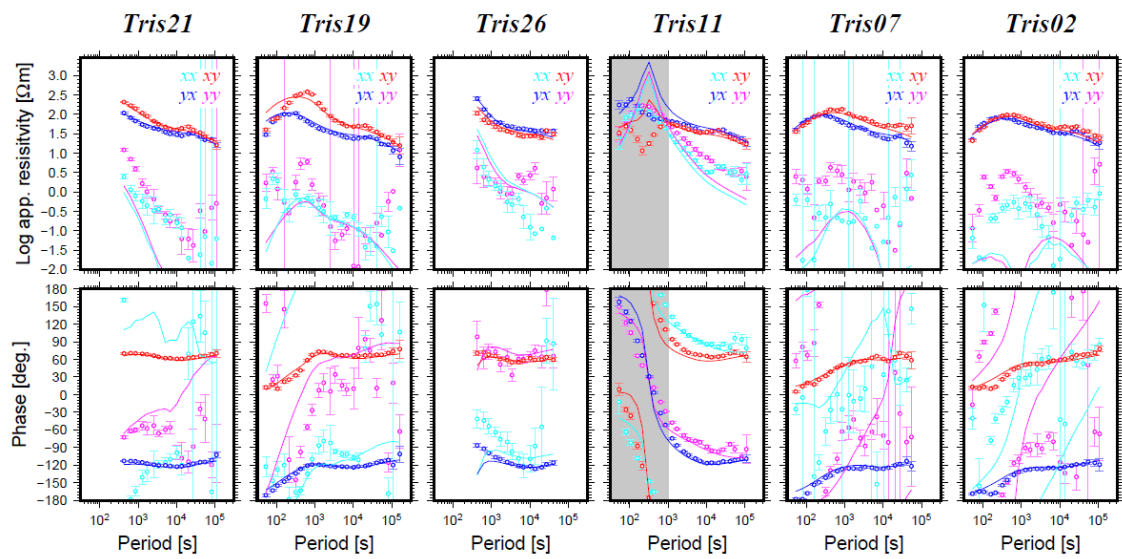


Fig. 2

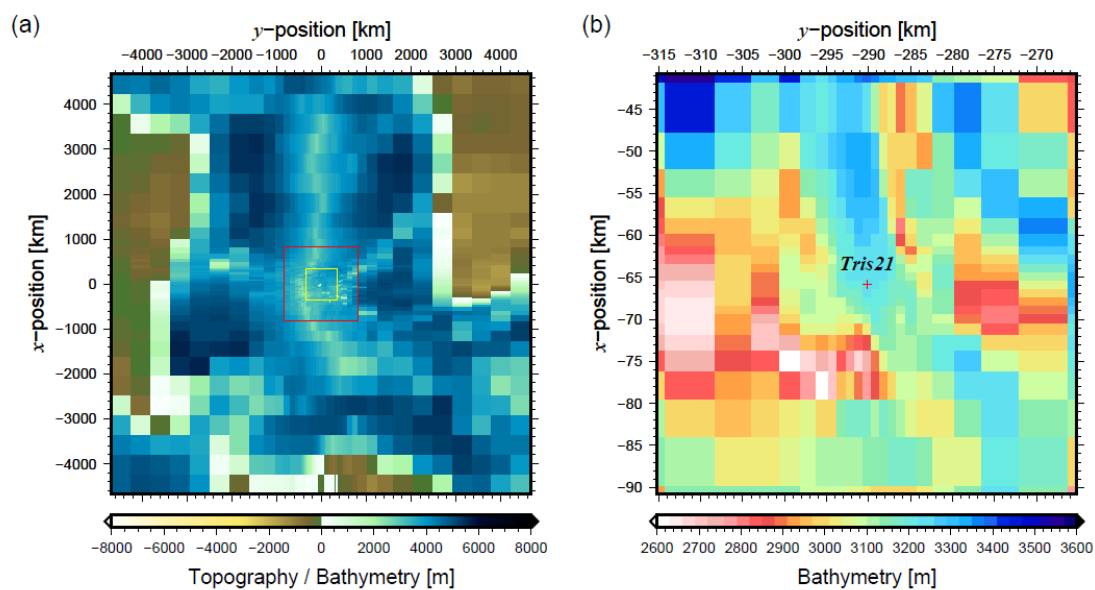


Fig. 3

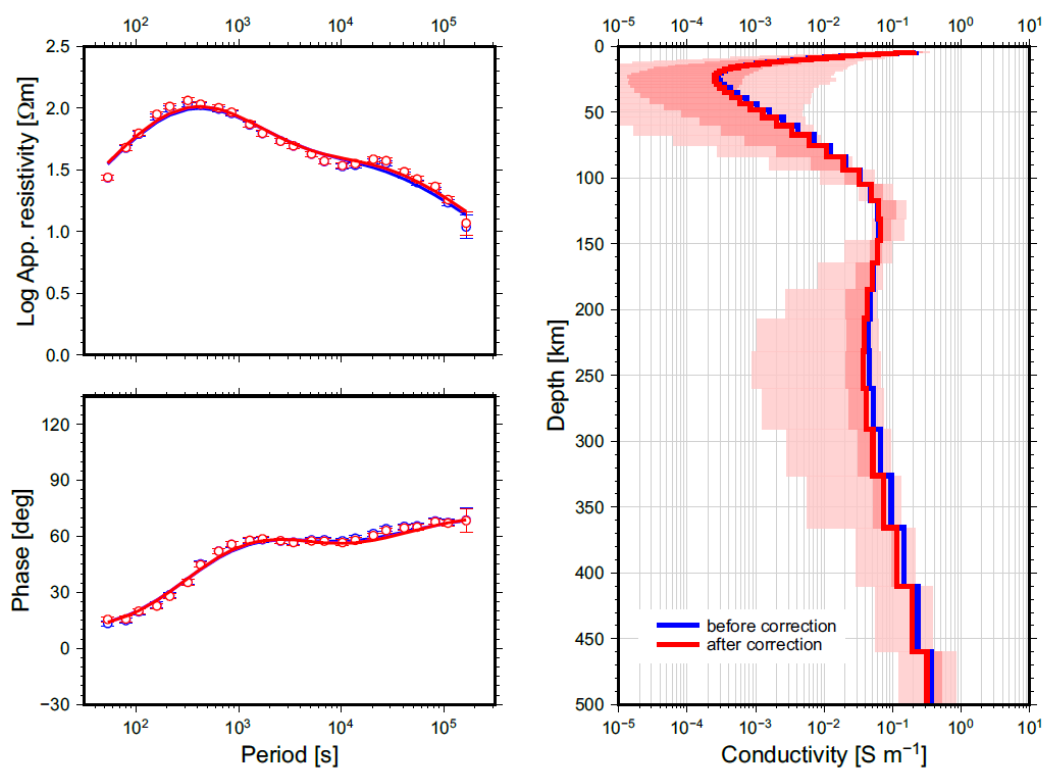


Fig. 4

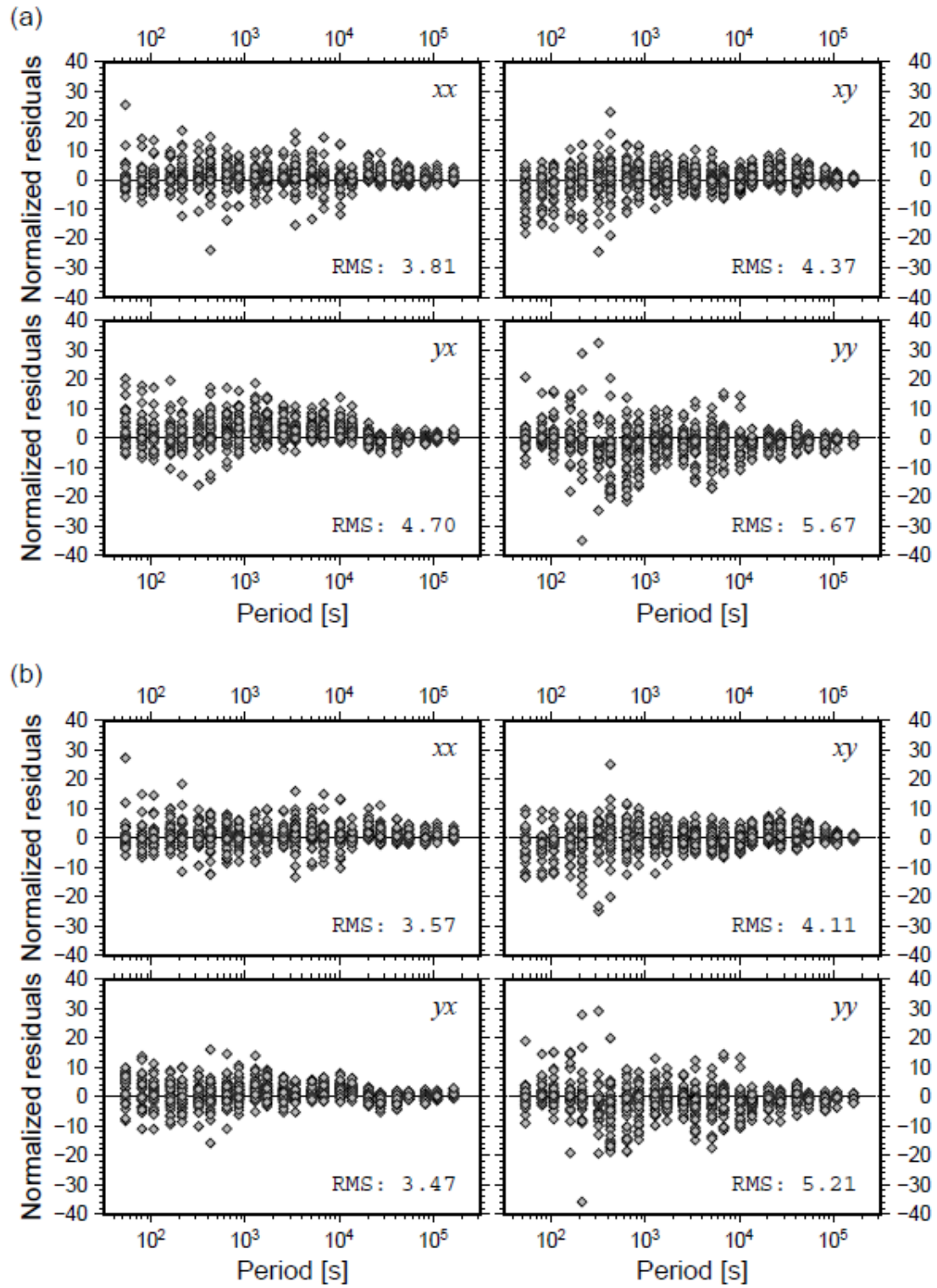


Fig. 5

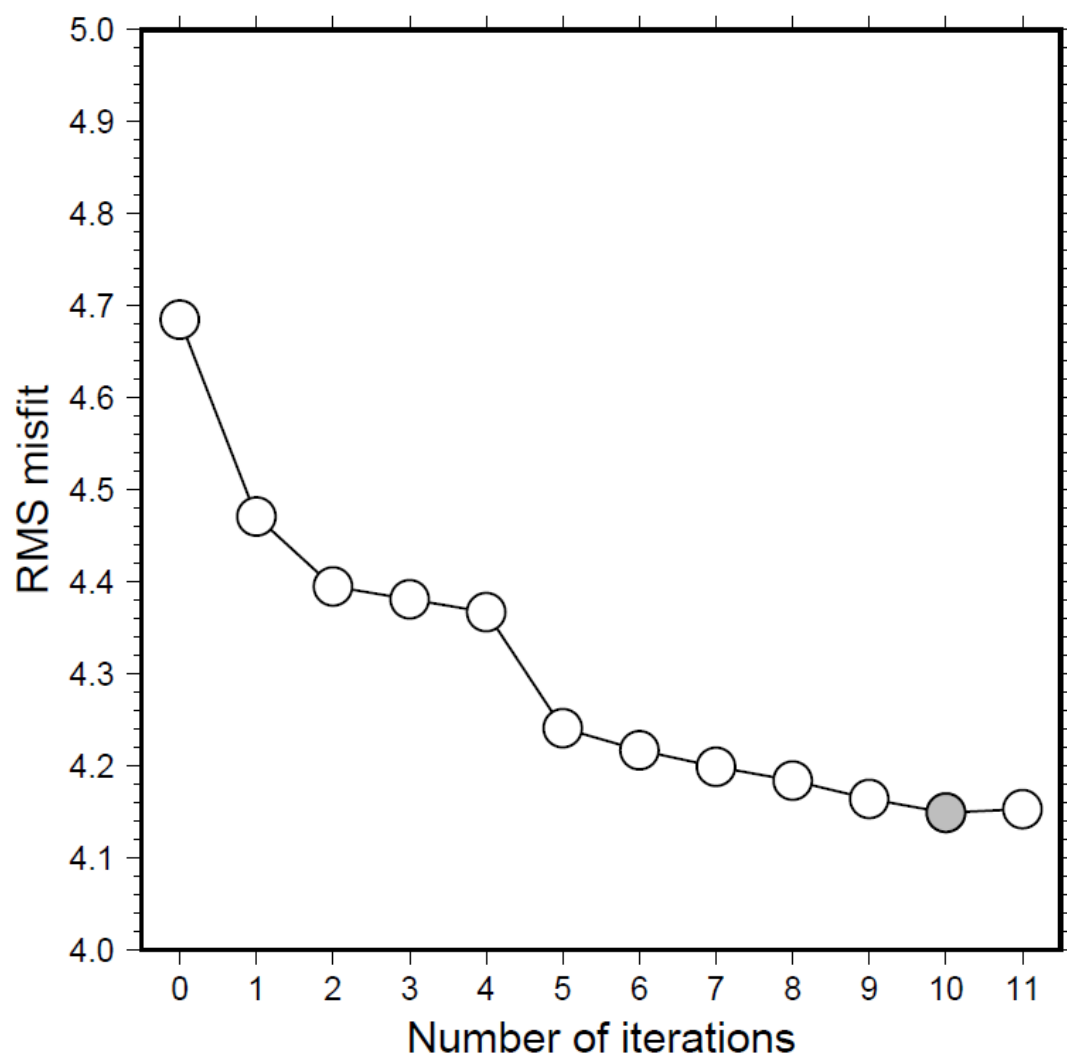


Fig. 6



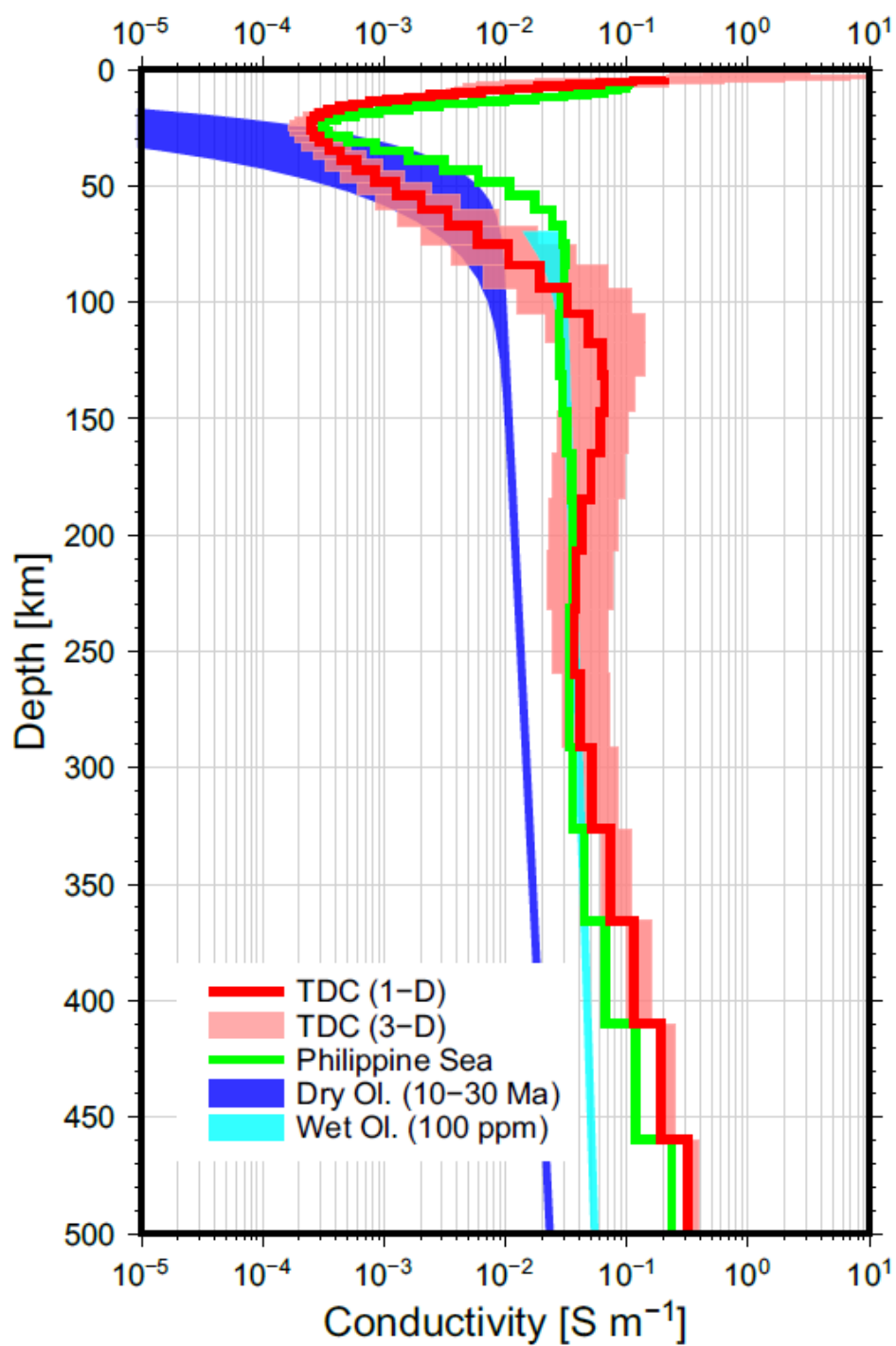


Fig. 8

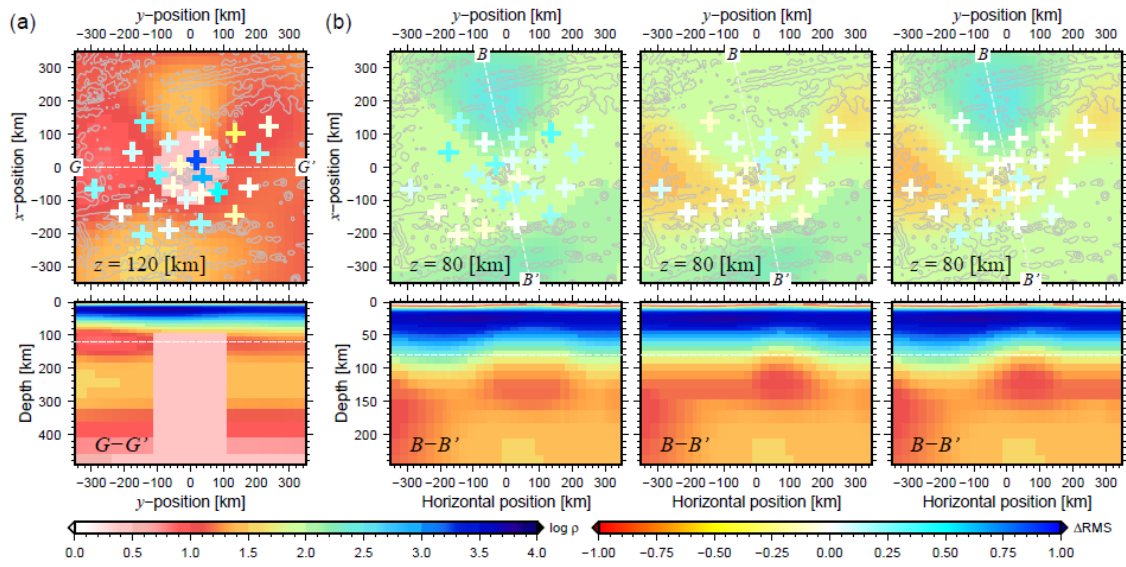


Fig. 9

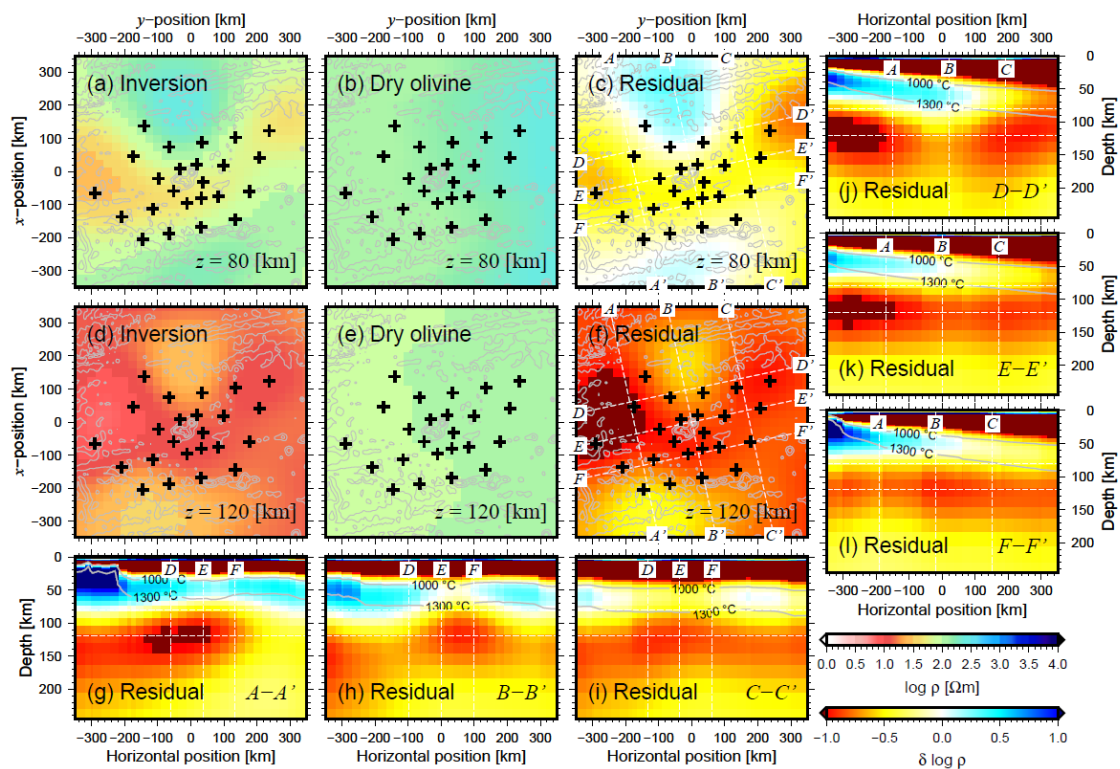


Fig. 10

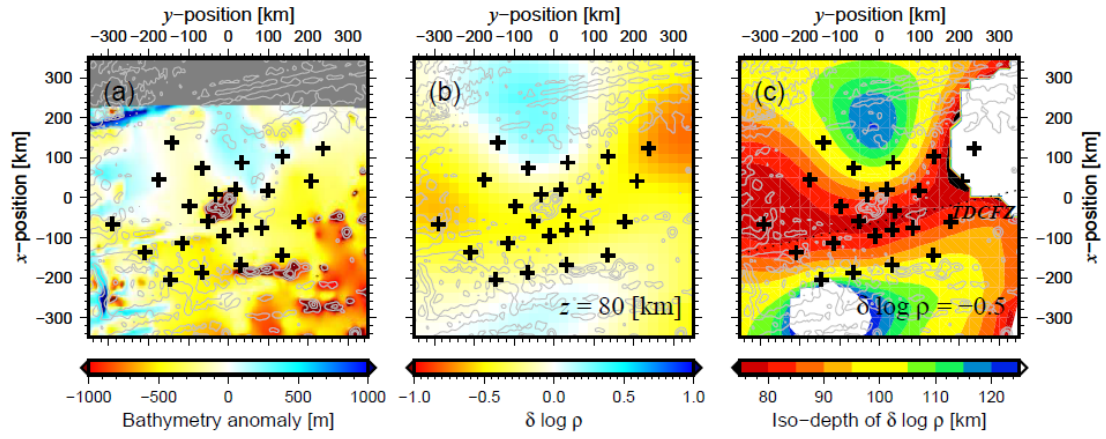


Fig. 11

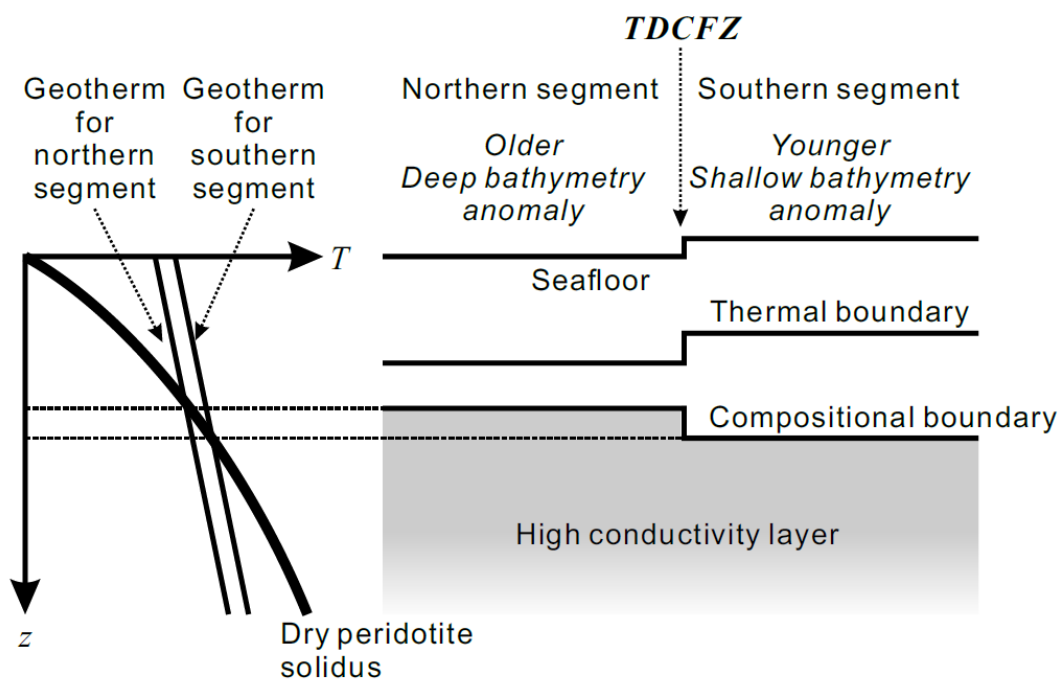


Fig. 12

Table 1. List of site locations and data status.

Site ID	Institute	Latitude	Longitude	Depth* (m)	Sampling Interval (s)	Available field components	Combination (<i>E</i> site/ <i>M</i> site)
Tris01	GEOMAR	35° 55.77' S	9° 40.90' W	3938	10	<i>E, M</i>	Tris01/Tris01
Tris02	GEOMAR	36° 40.21' S	9° 59.39' W	3637	10	<i>E, M</i>	Tris02/Tris02
Tris03	GEOMAR	37° 35.69' S	10° 18.14' W	3369	10	<i>E, M</i>	Tris03/Tris03
Tris04	ERI	38° 21.62' S	10° 46.56' W	3536	60	<i>E, M</i>	Tris04/Tris04
Tris05	GEOMAR	38° 34.78' S	11° 57.55' W	3155	10	<i>M</i>	Tris05/Tris06
Tris06	GEOMAR	37° 44.68' S	11° 22.17' W	3564	10	<i>E, M</i>	Tris06/Tris06
Tris07	GEOMAR	36° 54.26' S	11° 12.13' W	3816	10	<i>E, M</i>	Tris07/Tris07
Tris08	ERI	36° 07.80' S	10° 48.29' W	3947	60	<i>E, M</i>	Tris08/Tris08
Tris09	GEOMAR	35° 38.33' S	11° 29.62' W	4169	10		
Tris10	GEOMAR	36° 16.45' S	11° 56.21' W	3722	10	<i>E, M</i>	Tris10/Tris10
Tris11	ERI	36° 52.74' S	12° 06.95' W	3578	10, 60 [†]	<i>E, M</i>	Tris11/Tris11
Tris12	GEOMAR	37° 21.52' S	11° 53.81' W	3674	10	<i>E, M</i>	Tris12/Tris12
Tris13	ERI	37° 47.66' S	11° 57.16' W	3278	10, 60 [†]	<i>E, M</i>	Tris13/Tris13
Tris14	GEOMAR	37° 55.73' S	12° 26.89' W	3295	10	<i>E, M</i>	Tris14/Tris14
Tris15	ERI	38° 45.32' S	13° 04.72' W	3179	60	<i>E, M</i>	Tris15/Tris15
Tris16	GEOMAR	38° 54.16' S	14° 00.27' W	3117	10	<i>E, M</i>	Tris16/Tris16
Tris17	GEOMAR	38° 04.83' S	13° 38.07' W	3391	10	<i>E, M</i>	Tris17/Tris17
Tris18	GEOMAR	37° 35.80' S	12° 54.52' W	3153	10	<i>M</i>	Tris18/Tris19
Tris19	ERI	37° 15.43' S	13° 24.98' W	3595	10, 60 [†]	<i>E, M</i>	Tris19/Tris19
Tris20	GEOMAR	38° 16.61' S	14° 43.04' W	3224	10	<i>M</i>	Tris20/Tris16
Tris21	ERI	37° 36.84' S	15° 36.74' W	3229	60	<i>E, M</i>	Tris21/Tris21
Tris22	GEOMAR	37° 24.69' S	14° 33.17' W	3345	10		-
Tris23	GEOMAR	36° 38.61' S	14° 16.74' W	3678	10	<i>M</i>	Tris23/Tris24
Tris24	ERI	35° 49.11' S	13° 52.91' W	3658	60	<i>E, M</i>	Tris24/Tris24
Tris25	GEOMAR	36° 23.92' S	13° 02.91' W	3558	10	<i>M</i>	Tris25/Tris10
Tris26	GEOMAR	36° 59.49' S	12° 40.72' W	3527	10	<i>E, M</i>	Tris26/Tris26
NTG	GFZ	37° 25.08' S	12° 28.60' W	-57	1-		

*The value was taken from the MBES data at each site.

[†]Sampling intervals were changed in the middle of observation (see text for the detail).

E : electric field, M : magnetic field

ACCEPTED MANUSCRIPT

Table 2. List of the RMS misfits for our best model and the models modified for the sensitivity tests (see Figure 9 and text).

Model	RMS misfits				
	Total	xx	xy	yx	yy
Best model	4.15	3.57	4.11	3.47	5.21
Modified model A	4.28	3.63	4.32	3.79	5.20
Modified model B1	4.26	3.64	4.06	3.86	5.29
Modified model B2	4.18	3.62	4.17	3.43	5.24
Modified model B3	4.17	3.55	4.17	3.48	5.22